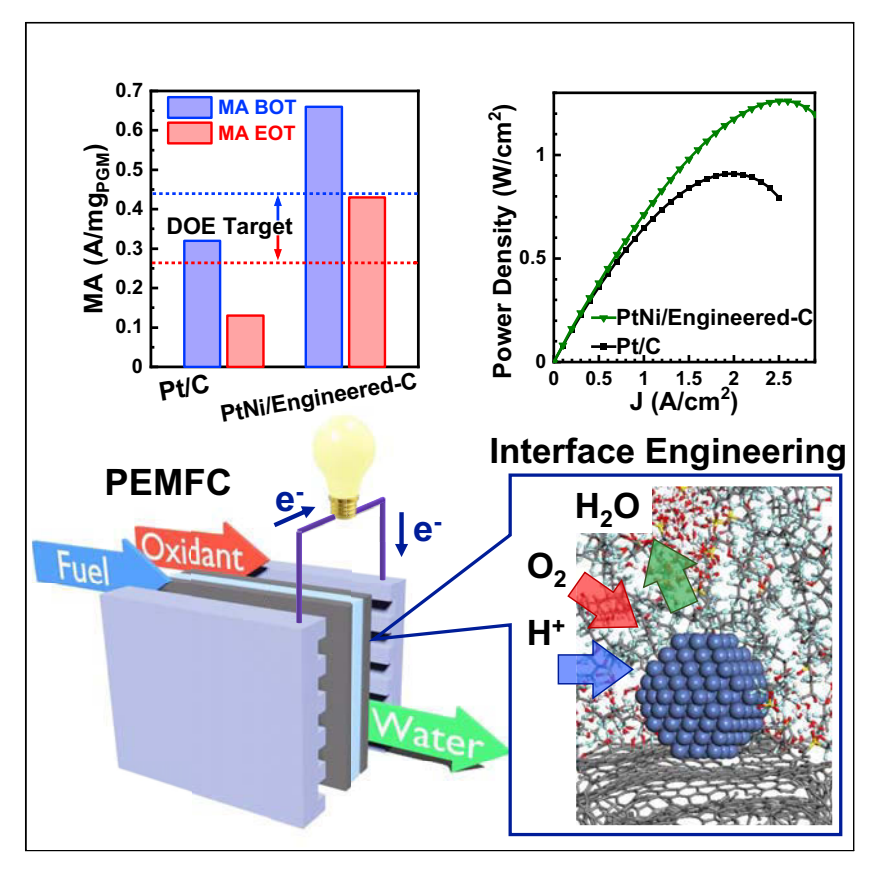
Matter



Article

Tailoring a Three-Phase Microenvironment for High-Performance Oxygen Reduction Reaction in Proton Exchange Membrane Fuel Cells



The oxygen reduction reaction (ORR) in proton exchange membrane fuel cells (PEMFCs) is sluggish and demands high use of Pt-catalysts, which drives up the system cost and limits its mass applications. Facilitating the ORR in PEMFCs, which occurs at a catalyst–electrolyte–gas three-phase interface, requires both active catalyst and efficient mass transport; however, reports on the latter are limited. This work demonstrates high PEMFC performances by creating a desirable ORR interface by engineering the surface of carbon supports.



Zipeng Zhao, Md Delowar Hossain, Chunchuan Xu, ..., Xiangfeng Duan, William A. Goddard III, Yu Huang

yhuang@seas.ucla.edu

HIGHLIGHTS

Carbon support surface can be manipulated to create a desirable reaction interface

Mass transport in PEMFCs is improved via carbon support engineering

Pt-based catalyst on improved carbon support showing outstanding performance in MEA

Zhao et al., Matter 3, 1774–1790 November 4, 2020 © 2020 Elsevier Inc. https://doi.org/10.1016/j.matt.2020.09.025







Article

Tailoring a Three-Phase Microenvironment for High-Performance Oxygen Reduction Reaction in Proton Exchange Membrane Fuel Cells

Zipeng Zhao,¹ Md Delowar Hossain,^{2,3} Chunchuan Xu,⁴ Zijie Lu,⁴ Yi-Sheng Liu,⁵ Shang-Hsien Hsieh,⁶ Ilkeun Lee,⁷ Wenpei Gao,⁸ Jun Yang,⁴ Boris V. Merinov,² Wang Xue,⁹ Zeyan Liu,¹ Jingxuan Zhou,¹ Zhengtang Luo,³ Xiaoqing Pan,^{8,10} Francisco Zaera,⁷ Jinghua Guo,^{5,11} Xiangfeng Duan,^{9,12} William A. Goddard III,² and Yu Huang^{1,12,13,*}

SUMMARY

Despite tremendous progress in catalyst development for ratelimiting cathodic oxygen reduction reaction (ORR), reducing Pt usage while meeting performance requirements in practical proton exchange membrane fuel cells (PEMFCs) remains a challenge. The ORR in PEMFCs occurs at a catalyst-electrolyte-gas three-phase interface. A desirable interface should exhibit highly active and available catalytic sites, as well as allow efficient oxygen and proton feeding to the catalytic sites and timely removal of water to avoid interface flooding. Here, we report the design of a three-phase microenvironment in PEFMCs, showing that carbon surface chemistry can be tuned to modulate its interaction with the ionomers and create favorable transport paths for rapid delivery of both reactants and products. With such an elaborate interfacial design, for the first time we have demonstrated PEMFCs with all key ORR catalyst performance metrics, including mass activity, rated power, and durability, surpassing the US Department of Energy targets.

INTRODUCTION

Proton exchange membrane fuel cells (PEMFCs) are of immense interest as a zero emission, quiet, mobile power source for automobiles, drones, submarines, and autonomous underwater vehicles. 1-3 Platinum (Pt) group metals (PGMs), particularly Pt, are typically used as the catalysts in commercial PEMFCs, in particular as the cathode catalyst for boosting the sluggish oxygen reduction reaction (ORR).³ Reduction of PGM usage in PEMFCs is essential to lower the cost and to enable more widespread adoption.^{4,5} To this end, intensive efforts have been devoted to developing new generation of electrocatalysts with greatly increased mass activities. 6-10 However, such high mass activities are usually only achieved in the half-cell rotating disc electrode (RDE) test, in which the mass transport limitation is compensated for by using the Koutecký-Levich equation, and represent the fundamental material limitation of this new generation of electrocatalysts. To date, the performance advancements achieved in the half-cell RDE test are difficult to achieve in practical PEMFCs; thus, the power density target set by the US DOE for PEFMCs is rarely met or addressed. Overall, despite tremendous progress in the development of catalysts, the reduction of PGM loading in practical PEMFCs (e.g., to meet the United States DOE target of a cathode loading level of \leq 0.1 mg_{PGM}/cm²) has met with much less success.5

Progress and Potential

The rate-limiting cathodic oxygen reduction reaction (ORR) in proton exchange membrane fuel cells (PEMFCs) occurs at a catalystelectrolyte-gas three-phase interface. A desirable interface should exhibit not only highly active and available catalytic sites, but also efficient mass transfer to allow timely reactant feeding and timely product removal. In this study, we demonstrate that carbon support surface chemistry can be tuned to modulate its interaction with the ionomers and hence create a favorable environment to facilitate ORR in membrane electrode assembly (MEA), and also demonstrate that the MEAs built with such a catalyst/support interface can deliver a performance surpassing the targets set by the US Department of Energy in terms of mass activity, stability, and rated power. This work demonstrates and highlights the importance of engineering a support-electrolyte interface to improve ORR in a realistic environment.







The ORR in a practical PEMFC occurs at a catalyst-electrolyte-gas three-phase interface. The challenge is multifaceted, involving the activity of catalysts, available active sites, and concerted transport of oxygen and proton through the polymer electrolyte (ionomer) to reach the active sites and to remove water from these sites. 11 The reduction of PGM loading causes a reduction in the number of catalytic sites. A higher reaction rate is thus needed for each catalytic site to sustain the overall power output, which in turn requires faster delivery of the reactants to, and removal of the product from, each active site. Because of this, mass transport resistance starts to play an increasingly limiting role in the electrodes, with lower PGM loading.^{5,12} To this end, an elaborate catalyst-electrolyte-gas three-phase interface design is necessary to facilitate the relevant mass transport processes for efficient ORR. As well as a highly active and durable Pt-based catalyst, 13-17 gas permeation, 18-20 proton conduction, ^{21,22} and water removal²³ are all equally important. Therefore, a desirable three-phase interface must include an efficient ORR catalyst with high intrinsic activity, while simultaneously allowing for rapidly feeding reactants (O2 and proton) without starving the reaction and for the timely removal of the product (water) to avoid flooding of the interface. This rarely addressed issue is the subject of this study.

Recognizing that the ionomers are mostly in contact with the carbon support, here we focus on chemical modification of the carbon support to tailor carbon-ionomer interactions to create a favorable three-phase interface to facilitate the ORR in PEMFCs. Specifically, we used a series of carbon materials with different surface oxygen contents (2.4%, 3.8%, and 12.0%, respectively) as the catalyst support to prepare cathode catalysts for use in membrane electrode assembly (MEA). Our systematic studies demonstrate that the catalysts supported on carbon with 2.4% surface oxygen display a state-of-the-art mass activity (MA) among all PGM-based (with PGM as the only active sites) MEAs reported to date. For the first time, this has enabled PEMFCs displaying all key ORR catalyst performance metrics, including MA, rated power, and durability, exceeding the targets set by the US DOE. Our molecular dynamics (MD) simulations suggest that an optimal surface oxygen ratio on the carbon surface leads to favorable carbon-ionomer interactions 24,25 and a microenvironment comprising both hydrophobic and hydrophilic paths, 26 which simultaneously allow the efficient shuttle of oxygen molecules and protons to, and timely removal of water from the catalytic sites, providing a desirable microenvironment for highly efficient ORR.²⁷

RESULTS AND DISCUSSION

To explore the impact of surface oxygen in carbon supports on ORR, we prepared catalysts on three types of carbon materials, each with a different surface oxygen ratio (labeled as C1, C2, and C3). We used synchrotron-based near-edge X-ray absorption fine structure (NEXAFS) spectroscopy to determine the ratio of surface oxygen on the surface of each carbon support. The carbon K-edge intensities are comparable for all samples (Figure 1A), suggesting identical carbon loading, whereas the oxygen K-edge intensity indicates that the oxygen ratio (i.e., oxygen to carbon (O/C) ratio for simplicity of description in this work) qualitatively follows a trend of C1 > C2 > C3 (Figure 1B). In addition, components corresponding with C=O, COOH, C=OH vibration modes are identified in both carbon K-edge and oxygen K-edge spectra, suggesting the presence of various forms of oxygen on the surface. ^{28–30} The oxygen-containing surface functional groups are also demonstrated by attenuated total reflection (ATR) Fourier transform infrared spectroscopy (FTIR). The band at \sim 1,750 cm $^{-1}$ can be assigned to C=O, while the band from 1,000

¹Department of Materials Science and Engineering, University of California, Los Angeles, Los Angeles, CA 90095, USA

²Materials and Process Simulation Center, California Institute of Technology, Pasadena, CA 91125. USA

³Department of Chemical and Biological Engineering, The Hong Kong University of Science and Technology, Clear Water Bay, Kowloon 999077, Hong Kong

⁴Ford Motor Company, Dearborn, MI 48121, USA

⁵Advanced Light Source, Lawrence Berkeley National Laboratory, Berkeley, CA 94720, USA

⁶National Synchrotron Radiation Research Center (NSRRC), 101 Hsin-Ann Road, Hsinchu Science Park, Hsinchu 30076, Taiwan

⁷Department of Chemistry and UCR Center for Catalysis, University of California, Riverside, Riverside, CA 92521, USA

⁸Department of Materials Science and Engineering, University of California, Irvine, Irvine, CA 92697, USA

⁹Department of Chemistry and Biochemistry, University of California, Los Angeles, Los Angeles, CA 90095, USA

¹⁰Department of Physics and Astronomy, University of California, Irvine, Irvine, CA 92697,

¹¹Department of Chemistry and Chemical Biology, University of California, Santa Cruz, Santa Cruz, CA 95064, USA

¹²California NanoSystems Institute, University of California, Los Angeles, Los Angeles, CA 90095,

¹³Lead Contact

*Correspondence: yhuang@seas.ucla.edu https://doi.org/10.1016/j.matt.2020.09.025





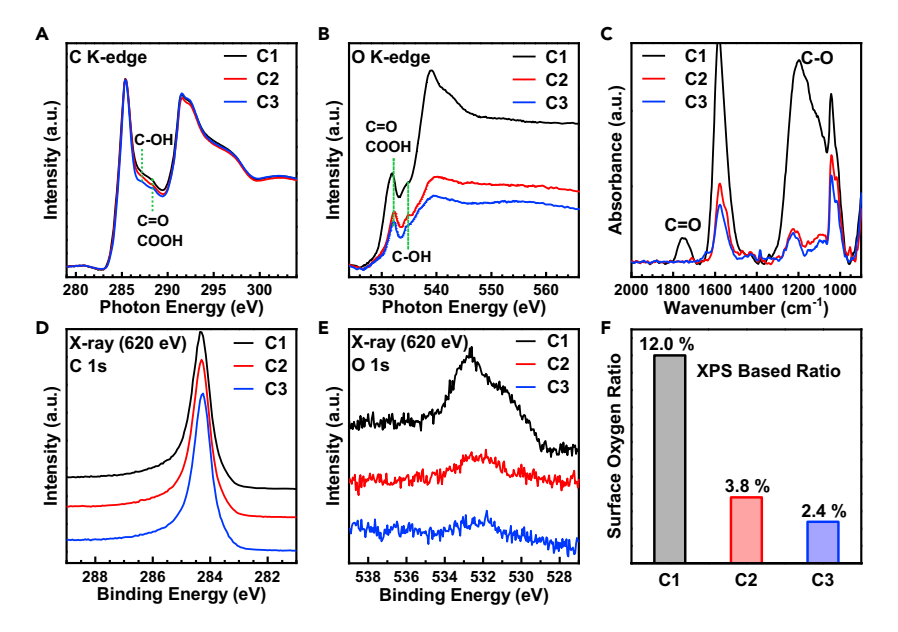


Figure 1. Characterization of Carbon Materials

(A and B) Synchrotron-based NEXAFS spectra for carbon K-edge (A) and for oxygen K-edge (B). The intensity is normalized by sample loading.

- (C) ATR-FTIR spectra.
- (D and E) Synchrotron-based XPS spectra for carbon 1s (D) and oxygen 1s (E).
- (F) The surface oxygen to carbon ratio for three carbon samples evaluated; C1, C2, and C3.

to 1,300 cm⁻¹ can be assigned to C–O. We find that the sum of both intensities follows the trend of C1 > C2 > C3 (Figure 1C, full spectra presented in Figure S1). $^{31-33}$ The quantitative ratio of surface oxygen was obtained via synchrotron-based X-ray photoelectron spectroscopy (XPS). The incident beam energy was fixed at 620 eV, resulting in inelastic mean free paths of about 0.6 and 1.2 nm for the oxygen 1s and carbon 1s photoelectrons generated, respectively.³⁴ The surface oxygen ratios were estimated to be 12.0%, 3.8%, and 2.4% for C1, C2, and C3, respectively (Figures 1D-1F). The overall elemental ratio was obtained using a CHNS analyzer (Table S1); the results showed the same trend for overall oxygen to carbon ratio (C1 > C2 > C3). Apart from the oxygen ratio, other key properties of all three carbon materials were comparable. The hydrophobicity of the above carbon materials was estimated using contact angle measurement (Figure S2). The trend hydrophobicity was C3 > C2 > C1, corresponding to a surface oxygen ratio of C1 > C2 > C3. Transmission electron microscopy (TEM) images revealed that C1, C2, and C3 show similar morphology of carbon spheres with an average diameter of 30 nm (Figure S3A). X-ray powder diffraction (XRD) patterns also show identical features, suggesting that these carbon materials share the same layered carbon structure and interplanar distance (Figure S3B; Table S2). The N2 adsorption/desorption tests also revealed similar Brunauer-Emmett-Teller (BET) surface areas (range 755–766 m²/g) and comparable pore size distributions for C1, C2, and C3 (Figures S3C and S3D; Table S2). However, further decreasing surface oxygen would lead to an observable change of pore distribution in the carbon structure (Figure S4), which would affect mass transport in the catalyst layer. 18

To investigate the impact of these carbon supports on fuel cell performance, we prepared PtNi ORR catalysts on these carbons (PtNi/C1, PtNi/C2, and PtNi/C3). Specifically, PtNi nanoparticles were directly grown on the respective carbon supports (C1,





C2, and C3) using a solution phase synthesis process. They were then annealed in a mixture of Ar and H_2 , followed by an acid wash and further annealing in Ar and H_2 (details given in the Experimental Procedures). TEM studies revealed that the PtNi nanoparticles on three different carbon supports exhibited a similar spherical morphology with a comparable average diameter of 4.9–5.0 nm (Figures S5 and S6). The XRD patterns of PtNi/C1, PtNi/C2, and PtNi/C3 are also comparable, which matches well with the comparable Pt ratios (72%–74%) revealed by energy dispersive spectroscopy (EDS) (Figure S6; Table S3). In addition, PtCo/C3 was also synthesized with a similar catalyst size for comparison (Figures S5 and S6). The metal loading within the catalyst was obtained by using inductively coupled plasma atomic emission spectroscopy (ICP-AES), which revealed a Pt loading in the range of 33–36 wt % for prepared catalysts (Table S4). These catalysts were tested using an RDE system for preliminary screening of the ORR performance (Figure S7; Table S5), in which they showed comparable half-cell performance.

The MEA was prepared by coating the obtained catalysts directly on the proton exchange membrane as the cathode layer using an ultrasonic spray system. The catalyst-coated membrane (CCM), gas diffusion layer (GDL), and gasket were assembled in a fuel cell fixture (details given in the Experimental Procedures). The Pt loading in all prepared MEAs was fixed at 0.10 and 0.05 mg_{PGM}/cm² for the cathode and anode, respectively. The MEAs used in our prepared catalysts showed a comparable roughness factor (Table S6). For a fair comparison, with the exception of the cathode layer catalyst, all materials used were the same in all prepared MEAs. Thus, the MEAs were labeled by the type of cathode catalyst used. All performance metrics in the MEAs, including ORR MA, rated power, and durability, etc., were tested and evaluated following the published DOE guidelines (details about DOE target and technique notes are given in the Experimental Procedures; Tables S7 and S8).

First, the MA of ORR catalysts in MEA was evaluated by normalizing the iR-free currents at 0.9 V in the $\rm H_2/O_2$ test by the cathode PGM mass. The beginning of test (BOT) MAs are 0.45, 0.56, and 0.66 A/mg_{PGM} for PtNi/C1, PtNi/C2, and PtNi/C3, respectively (Figure 2A; Table S7). It is important to note that, although the PtNi nanocatalysts used in these different MEAs showed comparable ORR MAs in the RDE half-cell test (Figure S7; Table S5), the ORR MAs observed in MEAs (Figure 2A) showed notable differences, indicating that the mass transport in these MEAs, rather than intrinsic catalytic activity, play a controlling role in the overall performance. Therefore, the observed trend of MA in PtNi/C1 < PtNi/C2 < PtNi/C3 indicates more efficient mass transport in PtNi/C3 compared with PtNi/C2 and PtNi/C1. Notably, the BOT MAs of the PtNi/C1, PtNi/C2, PtNi/C3, and PtCo/C3 all surpass the DOE target for MA (0.44 A/mg_{PGM}). Impressively, the MA of PtCo/C3 (0.72 A/mg_{PGM}) is about 2.3 times that of the MA (0.32 A/mg_{PGM}) of the benchmark Tanaka Kikinzoku Kogyo Pt/C and represents the state-of-the-art MA for PGM-based ORR catalysts achieved in MEA tests to date (Table S7).

The durability of the MEA performance is critical for long-term stable operation of practical PEMFCs. To test the practical durability of MEA performance with reasonable experimental time in a laboratory setting, the US DOE has recently suggested a standard accelerated durability test (ADT) protocol, in which a square wave potential between 0.60 and 0.95 V (3-s hold at each voltage) is applied to the MEA for 30,000 cycles with a targeted end of test (EOT) MA above 60% of BOT MA, and a minimum value above 0.26 A/mg_{PGM}. Although an ADT protocol with a triangle wave between 0.60 and 1.0 V (50 mV/s sweep rate) has been commonly used in previous studies, the newly suggested square wave protocol shows an acceleration factor five times





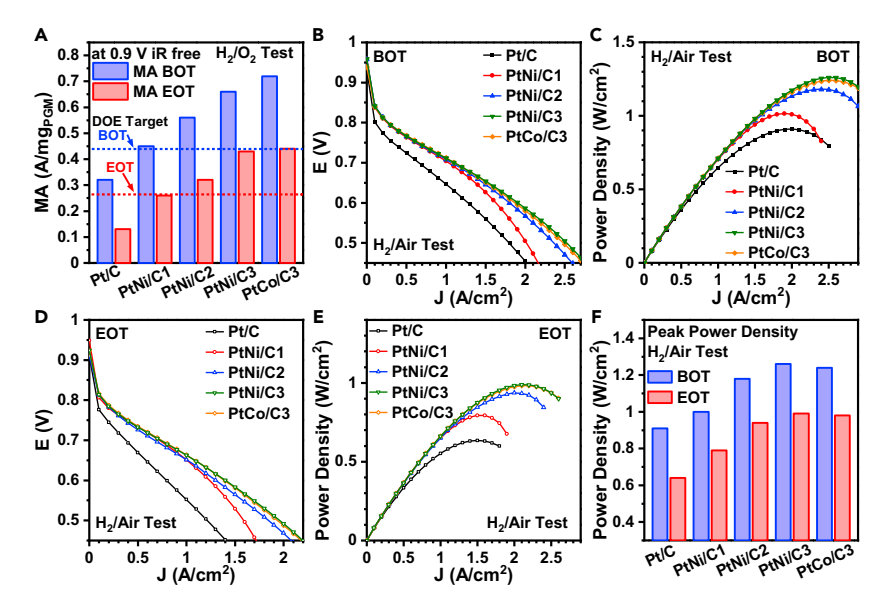


Figure 2. MEA Test

(A) Comparison of mass activities obtained in the H_2/O_2 test at the beginning of test (BOT; before ADT) and end of test (EOT; after ADT).

(B–E) H_2 /air test. (B) Polarization plots at BOT. (C) Power density plots at BOT. (D) Polarization plots at EOT. (E) Power densities plots at EOT.

(F) Comparison of peak power densities. The MEA test was performed at 80° C and 150 kPa_{abs} pressure unless specifically noted. This figure shows the average results of at least two MEAs.

that of the triangle wave protocol, and has been proven to be much harsher compared with the triangle wave protocol, which better reflects the long-term durability of the MEAs in practical devices. Notably, PtNi/C3 and PtCo/C3 MEAs all retain more than 60% of initial MA (DOE target) after 30,000 cycles of square wave ADT, and with EOT MA exceeding the DOE target. To the best of our knowledge, this is the first time that the MEA durability and EOT performance have exceeded the DOE target after the suggested square wave ADT, highlighting the long-term durability of our MEAs for practical PEMFCs. Notable much harsher compared wave ADT, highlighting the long-term durability of our MEAs for practical PEMFCs.

To further evaluate the performance of these MEAs in the working environment of a fuel cell, we next obtained the current/power polarization plot using air as an oxygen source (Figures 2B and 2C). We observed, at low current densities, that all our catalysts performed rather similarly and showed higher performance compared with Pt/C. At higher current density, where mass transport starts to play an increasingly important role, differences begin to appear for C1-, C2-, and C3-supported catalysts: a much obvious voltage drop was observed in PtNi/C1, while PtNi/C2, PtNi/ C3, and PtCo/C3 maintained a better performance in this mass transport region (Figure 2B). Such differences can be more clearly seen in the power density plots (Figure 2C). Power density values, in particular at high current densities, are good indicators for PEMFC performance related to the mass transport, including proton, oxygen transport, and water removal. The peak power densities of the prepared MEAs follow the trend of PtNi/C1 < PtNi/C2 < PtNi/C3 ≈ PtCo/C3 (Figures 2C and 2F), which is similar to the trend for MAs (Figure 2A), again supporting the idea that mass transport is more efficient in the C3-based catalyst layer in comparison with the C2-based catalyst layer, and much more efficient compared with the C1based catalyst layer. Thus, the performance differences observed in both H_2/O_2 and H₂/air tests can all be attributed to the different mass transport limitations related to





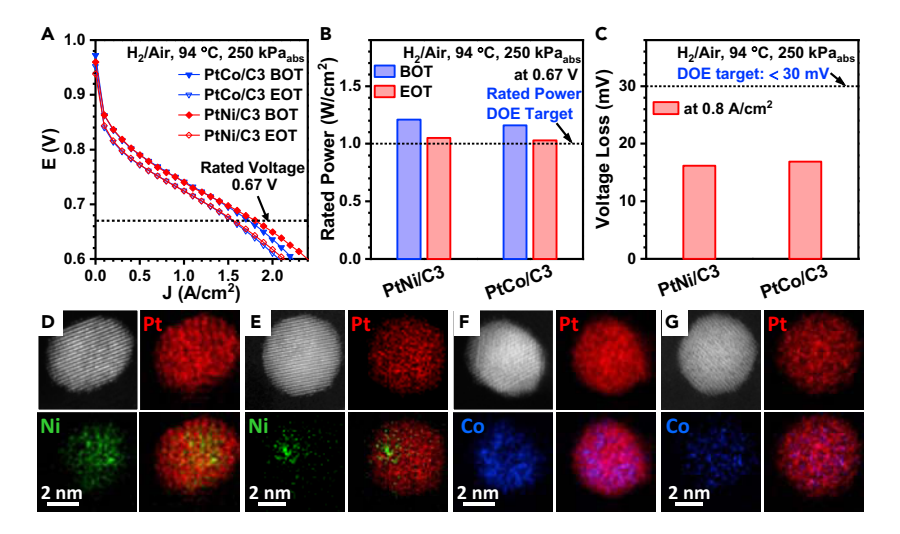


Figure 3. Rated Power of Representative MEAs and EDS Map Analysis of Cathode Catalysts (A) H_2 /air polarization plots obtained at the temperature of 94°C and pressure of 250 KPa_{abs} for rated power evaluation.

- (B) Comparison of rated power densities at BOT and EOT in for PtNi/C3, PtCo/C3.
- (C) Voltage loss from BOT to EOT at a fixed current density of 0.80 A/cm².

(D–G) STEM image and EDS elemental analysis of representative Pt-based nanoparticles. PtNi/C3 samples before the MEA test (D), and at EOT (E). PtCo/C3 samples before the MEA test (F), and at EOT (G). Each panel consists of the STEM image, mapping images of individual elements, and combined mapping of both elements.

the different carbon supports used. We further characterized the EOT performance following the aggressive square wave ADT protocol, suggested by the DOE, 35 to evaluate the durability of the MEAs. At the EOT, all MEAs based on our catalysts performed significantly better in comparison with Pt/C (Figures 2D and 2E). Compared with BOT, the EOT peak power density follows the same trend of PtNi/C1 < PtNi/C2 < PtNi/C3 \approx PtCo/C3 (Figures 2E, 2F, and S8).

We also evaluated the rated power of the MEAs, which takes into account heat rejection, and is an important aspect during the operation of fuel cells because the mass transport-induced power loss at high current density is converted to waste heat. Thus, the DOE has set a target of $Q/\Delta T < 1.45 \, \text{kW/°C}$ for heat rejection, which translates to the targeted rated power of >1 W/cm² measured at 0.67 V when the working temperature is 94°C. ¹⁸ Thus, the rated power is an important figure of merit directly reflecting the performance of practical fuel cells under working conditions, which is, however, rarely reported. Significantly, our PtNi/C3 and PtCo/C3 MEAs deliver a rated power of 1.21 and 1.16 W/cm², respectively, both above the DOE target (1 W/cm²) (Figure 3). Furthermore, the EOT rated power of both PtNi/C3 (1.05 W/cm²) and PtCo/C3 (1.03 W/cm²) remained above the DOE target after the square wave ADT (Figure 3B), showing significant promise for long-term stable operation. It is important to note that the rated power corresponds directly to the working performance of practical PEMFCs. Achieving the rated power target both before and after ADT clearly highlights the practical potential of our MEAs.

The voltage loss at a fixed current density from the BOT to EOT is another important measure characterizing the durability of the operation of the PEMFC. Significantly, the voltage losses for the PtNi/C3 and PtCo/C3 MEAs at 0.8 A/cm² after the square wave ADT were only 16.2 and 16.9 mV, respectively, far below the US DOE target (<30 mV) (Figure 3C). These evaluations attest to superior performance, in particular





the sustained high performance of the MEA after ADT, of these designed catalysts compared with previously reported catalysts (Table S8). 18,37 Although our studies have focused only on the catalyst layer, there are excellent examples in the literature for improving MEA rated power by optimizing the membrane, the ionomer, the GDL, or the gas flow pattern design. 38-40 For instance, we expect further enhancement may be achieved if the state-of-the-art Gore ultrathin membrane is used. 41

Furthermore, we performed TEM, scanning TEM (STEM), and EDS analysis on catalysts at EOT. The Pt/C exhibited significant size coarsening, with average size increasing from 3.8 \pm 1.1 nm (before the test) to 6.3 \pm 1.5 nm (EOT, after ADT), which can explain the 59% MA loss in the $\rm H_2/O_2$ test and the large voltage loss in the $\rm H_2/air$ test (Figures 2 and S9; Table S7). We also observed size coarsening in TEM images for the Pt alloy nanocatalysts, but to a much less degree. The sizes of the original PtNi nanocatalysts prepared on C1, C2, and C3 were 4.9 \pm 1.0, 4.9 \pm 1.0, and 4.9 \pm 1.1 nm, respectively, while the sizes of the corresponding PtNi nanoparticles after ADT were 6.1 \pm 1.7, 6.1 \pm 1.6, and 6.1 \pm 1.6 nm, respectively (Figure S5). The sizes of PtCo nanoparticles grown on C3 were 5.0 \pm 0.7 nm (before test) and 6.0 \pm 1.5 nm at EOT (Figure S5). The coarsening of nanocatalysts leads to a decrease in surface active sites, which contributes to the observed performance degradation at EOT.

In addition, we also observed a loss of non-noble transition metal in the evaluated catalysts at EOT. The atomic ratio of Ni drops from 28.1% to 11.2%, 26.7% to 10.8%, and 25.8% to 10.4% for PtNi/C1, PtNi/C2, and PtNi/C3, respectively. The atomic ratio of Co decreases from 17.9% to 10.7% for PtCo/C3 (Table S3). More interestingly, these nanocatalysts demonstrated excellent structural durability, as revealed in EDS elemental maps. The representative PtNi catalyst demonstrated a Pt-rich shell structure (Figure 3D), which has been suggested to be important for high durability in Pt alloy nanocatalysts. ⁴² The Pt-rich shell was retained at EOT but with increased thickness, as demonstrated by the EDS map (Figure 3E). Compared with the PtNi with a more concentrated Ni distribution in the core region, PtCo shares a similar core-shell structure with a Pt-rich shell, but Co is more dispersed in the PtCo nanocatalysts both before the MEA test and at EOT. The loss of Ni, Co is indicated by a comparison of the relative intensity change of Ni, Co in the EDS maps (Figures 3D–3G). It is noted that the leached metal cations may also poison the ionomers and contribute to the degradation of the performance after ADT (Figures 2D–2F). ⁴³

It is recognized that the three-phase interface is critical for MEA performance. ¹⁸ However, due to the complexity of the interface and lack of reliable characterization techniques, there is little atomic-scale insight on the three-phase interface, in particular the ionomer-substrate interface. For instance, the electron-beam-based techniques suffer from beam-induced damage on the ionomer. ^{44,45} Soft X-ray-based low radiation damage techniques provide the best resolution at the sub-15 nm scale, which is far from the resolution needed for capturing the nanometer-scale feature of the ionomer structure and distribution at the three-phase interface. ^{44,46} Therefore, we performed MD simulation to investigate the effect of the surface oxygen ratio in the carbon support on the interaction between the support and the perfluorosulfonic acid (PFSA) ionomers at the atomic scale. We also studied the impact of the above interactions on fuel cell performance.

To build the carbon support model, we equilibrated the amorphous carbon portion in the model using reactive force field (ReaxFF)-based MD calculations (using LAMMPS) (Figure \$10A). Then, we added three top layers of graphitic carbon on



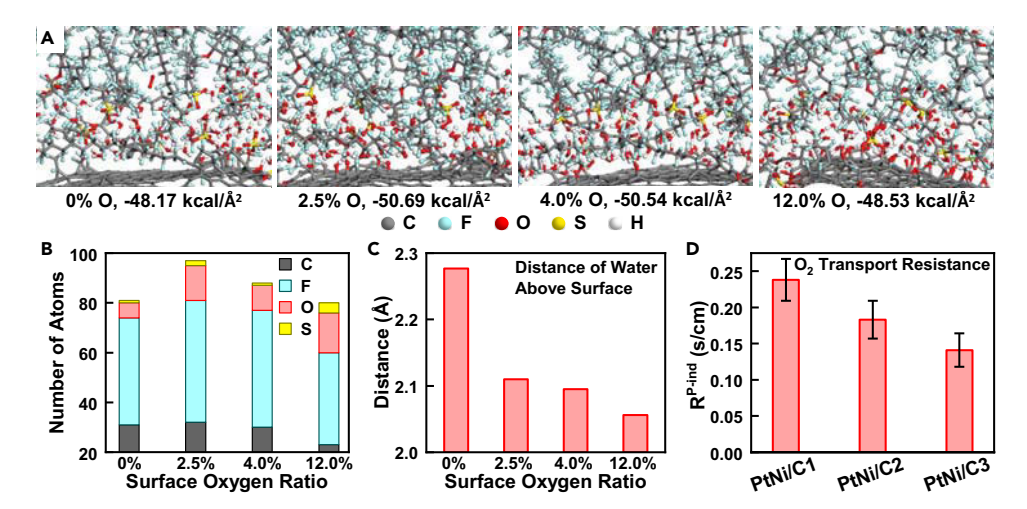


Figure 4. The Interfacial Interactions between the Carbon Surface and Hydrated PFSA Ionomers

(A) An image of the ionomer and water distribution on carbon surfaces after MD simulations. The bottom caption shows the interface energy between the ionomers and the carbon surface with different oxygen contents (0%, 2.5%, 4.0%, and 12.0%).

- (B) The number of atoms refers to the ionomer distributed within 0.3 nm distance above the carbon surfaces in simulation models (model size: 3.4 nm in width, 3.4 nm in depth).
- (C) The average distance of water molecules within 0.3 nm above the carbon surfaces.
- (D) Pressure independent parts of oxygen transport resistance measured at 80°C, RH 65% (details are given in the Experimental Procedures). The error bars represent standard error.

top of pre-equilibrated amorphous carbon to simulate the surface structure of carbon, as noted in the literature. ^{47,48} This core-shell carbon model leads to a predicted density of 2.15 g/cm³, with a predicted XRD pattern with the (002) peak at 26° and (100) peaks at 42° diffraction angles, which are in good agreement with experimental observations (Figure S3 and S10B). The top graphitic surface was then oxidized at four different surface oxygen ratios (0%, 2.5%, 4.0%, and 12.0%) with the distribution of C=O, C-OH, and COOH oxygenated functional groups based on experimental results. These sites are demonstrated by corresponding bonds detected in NEXAFS (Figures 1A and 1B). ^{28,30} We then equilibrated the predicted structure for 100 ps at 300 K (Figure S11) using ReaxFF reaction dynamics.

To describe the electrolyte, we used hydrated PFSA ionomers and equilibrated them at 600 K for 200 ps. The PFSA ionomer includes two portions, the polar or hydrophilic portion composed of sulfonic groups ($-SO_3^-$), and the non-polar or hydrophobic polytetrafluoroethylene (PTFE) backbone. To determine the interaction between the PFSA ionomers and the carbon surface, we used ReaxFF MD to equilibrate the hydrated PFSA ionomer structures on top of four different carbon surfaces at 300 K for 200 ps and then predicted their interaction energy (Figure S12). 40 The carbon surface with 2.5% oxygen showed a stronger interaction compared with other carbon surfaces (0%, 4.0%, or 12.0% oxygen) (Figure 4A; Table S9). It is also noted that the carbon with the 2.5% surface oxygen demonstrates the largest number of ionomer atoms within 0.3 nm of the carbon surface, which reflects the interface energy since those atoms contribute to the bonding between the ionomers and the carbon surface (Figure 4B). The stronger interaction between the hydrated PFSA ionomers and the carbon surface (2.5% oxygen) leads to a more uniform distribution of the ionomers, which in turn alleviates the known mass transfer issue in the catalyst layer due to an uneven distribution of the ionomers. 24,25 Indeed, the PtNi/C3 (C3





Table 1. Summary of DOE Technical Targets and the Performance Achieved in Our MEAs with a Tailored Three-Phase Microenvironment

Performance Metrics	Unit	DOE Target	PtNi/ C3	PtCo/ C3
Mass activity	A/mg _{PGM} @0.9 V iR free	>0.44	0.66	0.72
Loss in mass activity (EOT versus BOT)	%	<40	35	39
Rated power	W/cm ²	>1.00	1.21	1.16
Loss in voltage at 0.8 A/cm 2 (EOT versus BOT)	mV	<30.0	16.2	16.9

The cathode loading is maintained at 0.10 mg_{PGM}/cm² for all MEAs.

contains 2.4% surface oxygen) MEA displayed the smallest pressure-independent oxygen transport resistance (R^{P-ind}) (Figures 4D and S13).

In addition, our simulation shows that the water molecules are repelled further away from the carbon surface as the surface oxygen ratio decreases, as indicated by the average distance of water molecules above the carbon surface (within 0.3 nm) (Figure 4C). Thus, the simulation suggests that the carbon with a lower surface oxygen ratio may have less of a problem with water flooding of the interface in the MEA (Figure 4C), which may explain the better durability of PtNi/C3 compared with PtNi/C2 and PtNi/C1 since excess water and flooding can accelerate the degradation of the electrode.²³ The calculated results show that the carbon surface with 0% oxygen interacts only with the hydrophobic PTFE part of the PFSA ionomer (via C-F and C-C interactions) (Figure 4A). In contrast, the 12.0% oxygenated surface is highly hydrophilic and allows only the sulfonic group to bind on its highly oxygenated surface, with very few non-polar groups on the carbon sites (Figure 4A). In contrast, 2.5% and 4.0% oxygenated surfaces have both hydrophilic (sulfonic-oxygenated carbon) and hydrophobic (C-F and C-C) interactions within the interface (Figure 4A). Together, the C3 shows the strongest interactions with both hydrophilic and hydrophobic parts of the ionomers, which simultaneously promotes both O₂ and proton transfer: i.e., O_2 prefers a hydrophobic region (PTFE backbone) and diffuses through it quickly, while the proton (H_3O^+) and water prefer the hydrophilic part (sulfonic acid side chain) for fast diffusion. 49 Thus the most desirable three-phase interface should involve a combination of both the hydrophilic and hydrophobic interface near or next to the catalysts facilitating O_{ad} , OH_{ad} , and H_2O_{ad} formation.²⁷

Conclusion

Together, this work demonstrates that carbon surface chemistry plays a critical role in the MEA performance of Pt-based catalysts in practical PEMFCs. We showed that the Pt alloy nanocatalysts on carbon supports with an optimal surface oxygen ratio lead to state-of-the-art MEA performance, with all the key ORR performance metrics, including mass activities, rated power, and durability, exceeding the US DOE targets (Table 1). We attribute this outstanding performance to the favorable interaction between the carbon substrate and the ionomers, resulting in a more uniform distribution of ionomers in the catalyst layer and a desirable microenvironment involving both hydrophilic and hydrophobic paths that facilitate the balanced supply of protons and oxygen molecules to the catalytic sites, as well as the timely removal of water molecules from the interface. These findings highlight the critical role of the three-phase microenvironments in facilitating catalytic reactions in a complex system and open a new pathway to greatly boost the performance of practical PEMFCs.





EXPERIMENTAL PROCEDURES

Resource Availability

Lead Contact

Further information and requests for resources should be directed to and will be fulfilled by the Lead Contact, Prof. Yu Huang (yhuang@seas.ucla.edu).

Materials Availability

This study did not generate new unique reagents.

Data and Code Availability

Data supporting the findings of this paper are available within the article and its Supplemental Information files and from the Lead Contact upon reasonable request.

Chemicals and Materials

Platinum(II) acetylacetonate [Pt(acac)₂], nickel(II) acetylacetonate [Ni(acac)₂], nickel(III) acetate tetrahydrate [Ni(Ac)₂·4H₂O], cobalt(III) acetate tetrahydrate [Co(Ac)₂·H₂O], benzyl acid, Nafion dispersion, and Aquivion D83-06A ionomer dispersion were purchased from Sigma Aldrich. Bis(triphenylphosphine)dicarbonylnickel [(C₆H₅)₃P]₂Ni(CO)₂ was purchased from Alfa Aesar. N,N-Dimethylformamide (DMF), acetone, and isopropanol (IPA) were purchased from Fisher Scientific. Ethanol was purchased from Decon Labs, Inc. The SGL-29BC, the Freudenberg H23C8 GDL, and the PTFE gasket were purchased from The Fuel Cell Store. Carbon black (Ketjenblack EC-300J) was obtained from Fitz Chem LLC. Water used was Ultrapure Millipore (18.2 M Ω ·cm).

Preparation of Carbon Materials (C1, C2, C3, and C4)

C1 was prepared by annealing Ketjenblack EC-300J in air at 400°C to achieve an increased oxygen ratio on the carbon surface. C2 was the original Ketjenblack EC-300J. C3 and C4 were prepared by annealing Ketjenblack EC-300J in a gas mixture of argon (Ar) and hydrogen (H₂) at 800°C–1,000°C to achieve a reduced surface oxygen ratio.

Synthesis of PtNi/C (C can be C1, C2, or C3)

Solution Phase Synthesis

Carbon black (140 mg; C1, C2, or C3) and 28 mg $[(C_6H_5)_3P]_2Ni(CO)_2$ were dispersed in 135 mL DMF under ultrasonication for 30 min in a 325 mL pressure bottle (sealed); 190 mg Pt(acac)₂, 110 mg Ni(ac)₂·4H₂O, and 1,030 mg benzoic acid were dissolved in 25 mL DMF in a 20 mL vial. The prepared solution described above was then added to the 325 mL pressure bottle and mixed with carbon black and $[(C_6H_5)_3P]_2Ni(CO)_2$ solution. After ultrasonication for 5 min, the sealed pressure bottle was directly put into an oil bath at 140°C and then slowly heated to 160°C. The pressure bottle was kept at 160°C for 48 h. After the reaction was finished, the catalyst was collected by centrifugation, then dispersed and washed with IPA and an acetone mixture. The centrifugation and re-dispersion steps were repeated three times. Then the catalysts were dried in a vacuum at room temperature.

Acid Wash and Annealing

The dried catalyst was first annealed at 250°C for 2 h in an Ar and H_2 mixture (volume ratio of $\text{Ar/H}_2 = 500/1$). Then, about 200 mg of annealed catalyst was dispersed in 20 mL 0.2 M H_2SO_4 in a 25 mL vial. The dispersion was then purged with N_2 until N_2 saturation. The vial was kept in 85°C for 6 h. The catalyst was collected using centrifugation when the acid wash had finished, and then dispersed and washed with water. The centrifugation and re-dispersion steps were repeated three times.





Then, the catalysts were dried in a vacuum at room temperature, followed by annealing at 200° C for 2 h in the Ar and H₂ mixture (volume ratio of Ar/H₂ = 500/1).

Synthesis of PtCo/C3

Solution Phase Synthesis

Carbon black (140 mg; C3) was dispersed in 135 mL DMF under ultrasonication for 30 min in a 325-mL pressure bottle (sealed); 190 mg Pt(acac)₂, 140 mg Co(ac)₂· $4H_2O$, and 1,030 mg benzoic acid were dissolved in 25 mL DMF in a 20 mL vial. Then the prepared solution described above was added into the 325 mL pressure bottle and mixed with carbon black solution. After ultrasonication for 5 min, the sealed pressure bottle was directly put into an oil bath at 140°C and then slowly heated to 160°C. The pressure bottle was then kept at 160°C for 48 h. After the reaction was finished, the catalyst was collected by centrifugation, then dispersed and washed with IPA and an acetone mixture. The centrifugation and re-dispersion steps were repeated three times. Then the catalysts were dried in a vacuum at room temperature.

Acid Wash and Annealing

The dried catalyst was then annealed at 400°C for 2 h in the Ar and H_2 mixture (volume ratio of $\text{Ar/H}_2 = 500/1$). Then, about 200 mg of annealed catalyst was dispersed in $20 \text{ mL} \ 0.2 \text{ MH}_2 \text{SO}_4$ in a 25 mL vial. The dispersion was then purged with N_2 until N_2 saturation. The vial was kept at 85°C for 6 h. The catalyst was collected by centrifugation after the acid wash had finished, and then dispersed and washed with water. The centrifugation and re-dispersion steps were repeated three times. Then the catalysts were dried in a vacuum at room temperature. The dried catalyst was then annealed at 200°C for 2 h in the Ar and H_2 mixture (volume ratio of $\text{Ar/H}_2 = 500/1$).

Characterization

TEM images were taken using an FEI T12 transmission electron microscope operated at 120 kV. Atomic-resolution high-angle annular dark-field (HAADF) images, as well as EDS maps, were taken using a JEOL Grand ARM300CF scanning/transmission electron microscope operated at 300 kV. HAADF images were also taken using an FEI TITAN operated at 200 kV in STEM mode. The TEM/STEM sample grids were prepared by dispersing the sample in a mixture of water and ethanol, then dripping the dispersion onto carbon-coated aluminum grids (Ted Pella, Redding, CA) using a pipette, and drying under ambient conditions. XRD patterns were collected using a Panalytical X'Pert Pro Xray powder diffractometer with Cu- $K\alpha$ radiation. The concentration of catalysts was determined by ICP-AES (Shimadzu ICPE-9000) as well as by EDS coupled in an FEI Titan transition electron microscope. The data for the BET surface areas and pore distributions were acquired using a Micromeritics Tristar II 3020 surface area and porosity analyzer. ATR-FTIR spectra were recorded using a horizontal reflection ATR accessory (PIKE Technology, MIRacle, ZnSe crystal) and a DTGS detector coupled to an FTIR spectrometer (Bruker, Tensor 27). The spectra were the result of averaging data from 1,024 scans, taken with a 4 cm⁻¹ resolution. The synchrotron radiation-based high-resolution XPS measurements were carried out at Taiwan Light Source Beamline 09A1 of the National Synchrotron Radiation Research Center, Taiwan. The measurements were conducted at room temperature. The photon energy for XPS measurements was set at 620 eV. The photon energies were calibrated using the Au 4f core level signal emitted from a clean gold foil electrically connected to the samples. The intensities were normalized using the photoionization cross-section of each element to compare the surface oxygen to carbon ratio. NEXAFS spectroscopy measurements on carbon and oxygen K-edges were carried out on Beamline 7.3.1 at the Advanced Light Source, Lawrence Berkeley National Laboratory, CA. The energy resolution on carbon and oxygen K-edges was set to 0.2 eV and recorded in total electron yield mode with careful energy calibration before





and after the experiment. The measurement of contact angle used a First Ten Angstroms FTÅ100 contact angle analyzer. The sessile drop method was adopted. The sample was prepared by dispensing and drying liquid dispersion of carbon materials on an adhesive slide (ultrathin double-sided tape attached to a glass slide), similar to previously reported procedures. The CHNS analysis was performed on a Thermo Fisher Flash Smart Elemental analyzer (detection limit: 0.01%). The calculation of O assumes that the major component of carbon black is C, H, N, S, and O as noted in the literature.

Electrode Preparation and Electrochemistry Test

A typical catalyst ink was prepared by mixing 2 mg of catalyst powder (PtNi/C1, PtNi/C2, PtNi/C3, and PtCo/C3) with 2 mL of ethanol solution containing 16 μ L of Nafion (5 wt%) using an ultrasonication time of 5 min. The benchmark Pt/C ink was prepared by mixing 1.5 mg of Pt/C powder with 2 mL of ethanol solution containing 20 μ L of Nafion (5 wt%) using an ultrasonication time of 5 min. Then, 10 μ L of prepared ink was dropped onto a 5 mm diameter glassy carbon electrode (Pine Research Instrumentation). Estimation of PGM loading was based on the overall PGM ratio within the catalyst determined by ICP-AES. The ink was dried under an infrared lamp. The electrode was then ready for the electrochemical test.

A three-electrode cell was used to carry out the electrochemical measurements. The working electrode was a catalyst-coated glassy carbon electrode. An Ag/AgCl electrode was used as the reference electrode. Pt wire was used as the counter electrode. Cyclic voltammetry (CV) measurements were conducted in an N_2 -saturated 0.1 M HClO $_4$ solution between 0.05 and 1.1 V versus a reversible hydrogen electrode (RHE) at a sweep rate of 100 mV/s. The electrochemical active surface area (ECSA) was measured by integrating the hydrogen underpotential deposition (H $_{\rm upd}$) peak in CV, assuming 210 μ C/ cm $^2_{\rm PGM}$. ORR measurements were conducted in an O_2 -saturated 0.1 M HClO $_4$ solution between 0.05 and 1.05 V versus RHE at a sweep rate of 20 mV/s. ADT was performed in an oxygen-saturated 0.1 M HClO $_4$ solution by applying square wave potential sweeps between 0.6 and 0.95 V versus RHE (0.6 V 3s and 0.95 V 3s) for 30,000 cycles.

MEA Fabrication and Test

A series of catalysts were investigated as cathode catalyst layers in MEA testing. The catalyst inks were made by mixing the catalysts with the ionomer solution (Aquivion D83-06A) and a water-IPA solvent mixture, followed by sonicating the dispersion in ice water for 1.5 h. The fresh inks were then spray-coated onto the Johnson Matthey (JM) half-CCM using a Sono-Tek ultrasonic spray system. The anode catalyst layer on the JM half-CCM had a platinum loading of $0.05~{\rm mg_{PGM}~cm^{-2}}$, and the membrane thickness was 18 μm . The cathode catalyst loading was controlled to be 0.10 mg_{PGM} cm⁻², which was confirmed by ICP-AES measurements. The fabricated CCM was dried in a vacuum oven to completely evaporate the solvents. Two 3-mil PTFE sheets were pressed to make a gasket (total thickness: 6 mil). A GDL, which includes a microporous layer, was used (total thickness of 230 µm). Two GDLs, two gaskets, and the prepared CCM were pressed to make the MEA. Then, MEAs were loaded in Fuel Cell Technology 5 cm² single-cell hardware and tested in the Scribner 850e fuel cell test stand at 80°C and 150 kPa_{abs} (abs: absolute; all pressures noted in this work refer to the absolute pressure) and 100% relative humidity (RH), following the US DOE fuel cell test protocol. The gas flow rate was 1,500/2,000 sccm during H_2 /air and H_2 / O_2 test for the anode and cathode, respectively. The ADT for Pt-based catalysts was performed using a square wave voltage from 0.6 to 0.95 V with a duration of 3 s for each voltage level, according to the US DOE MEA ADT protocol for PGM-based catalysts. Each test was run up to 30,000 cycles at 80°C, 150 kPa_{abs}, 100% RH, with H₂/N₂ flow 100/100 sccm for the anode and cathode, respectively.





The performance metrics of the MEAs at the BOT and end of test (EOT), such as polarization curves, MA, ECSA, high-frequency resistance by alternating current impedance, and H $_2$ crossover, were recorded using a Scribner 850e fuel cell test station and a Scribner 885 potentiostat linked to the 850e fuel cell station. The ECSA was determined by integrating the H $_{\rm upd}$ peak in CV, assuming 210 μ C/cm $^2_{\rm PGM}$.

Rated Power Test for MEA

MEAs using PtNi/C3 or PtCo/C3 as a cathode catalyst were prepared in a similar way as described above. The BOT rated power of prepared MEA was tested in the Scribner 850e fuel cell test stand at 94°C, 250 kPa_{abs}, and 100% RH. ¹⁸ The H₂/air gas flow rate was 835/2,000 sccm for the anode and cathode, respectively. The durability test, which involved 30,000 cycles of square wave (0.6 V maintained 3s, 0.95 V maintained 3s) at 150 kPa_{abs} and 80°C, was performed for the tested MEA. The H₂/N₂ gas (100% RH) flow was 100/100 sccm for the anode and cathode, respectively. Then EOT rated power of the MEA was tested at 94°C, 250 kPa_{abs}, and 100% RH. The H₂/air gas (100% RH) flow rate was 835/2,000 sccm for the anode and cathode, respectively.

The US DOE assumes 90 kW stack gross power (P_{stack}) required for 80 kW net power and sets a heat rejection target, $Q/\Delta T_i$ of <1.45. The rated power was measured at A rated voltage (V_{rated}), which can be defined by Equation 1.¹⁸

$$\frac{Q}{\Delta T_i} = \frac{P_{stack}(1.25 - V_{rated})}{V_{rated}(T_{stack} - T_{ambient})}$$
(Equation 1)

The US DOE protocol assumes P_{stack} = 90 kW and $T_{ambient}$ = 40°C, if T_{stack} = 94°C, Q/ ΔT_i = 1.445, which meets the target (Q/ ΔT_i of \leq 1.45), the V_{rated} will be around 0.67 V. Thus, the rated power will be measured at 0.67 V. ¹⁸

Oxygen Transport Resistance Test for MEA

The MEA was tested at 80°C with 65% RH for both anode and cathode. Ultrahigh pure hydrogen was applied in the anode. The O_2 and N_2 gas mix was pre-mixed by Airgas, and the gas mix cylinders were used as a gas source. The dry O_2 mole ratios for pre-mixed gases were 0.981%, 1.491%, and 2.001%, as determined by Airgas. To identify the pressure-independent part of the total oxygen transport resistance, the test was performed at a total pressure of 110, 150, 190, 230, and 270 kPa_{abs}. The total oxygen transport resistance can be approximately obtained by Equation 2:

$$R_{\text{total}} = \frac{4FC_{O_2}}{i_{\text{lim}}} = \frac{4F}{i_{\text{lim}}} \times \frac{P_{\text{abs}} - P_{H_2O}}{RT} \times x_{O_2 - dry},$$
 (Equation 2)

where $R_{\rm total}^{\rm O_2}$ is the total oxygen transport resistance; $C_{\rm O_2}$ is oxygen concentration; $P_{\rm abs}$ is the total pressure; $P_{\rm H_2O}$ is the pressure of water vapor at the testing temperature; $x_{\rm O_2-dry}$ is the dry $\rm O_2$ ratio; and i_{lim} is the limit current density.

The limit current density was identified as the largest current density (considering the absolute value) obtained through linear voltage sweep (0.12–0.41 V, 2 mV/s) using the 885 potentiostat attached to the 850e fuel cell station. The total oxygen transport resistance can be separated into the pressure-dependent part (R^{P-d}) and the pressure-independent part (R^{P-ind}), which represents the Knudsen diffusion and diffusion of oxygen through the ionomer layer. ^{53,54} The relationship of total oxygen resistance (R_{total}), the pressure-dependent part of oxygen transport resistance (R^{P-ind}), and the pressure-independent part of oxygen transport resistance (R^{P-ind}) can be expressed in Equation 3:





$$R_{\text{total}} = R^{P-d} + R^{P-\text{ind}}$$
. (Equation 3)

Computational Details

The calculations were performed by using ReaxFF implemented in the MD package LAMMPS, ^{55,56} which differs from traditional unreactive force fields by

- Describing the electrostatic interactions using a distributed atom size charge on each atom that was allowed to change on every step of MD, allowing the electrostatic interaction to change as reactions occur
- Allowing all valence interactions to break, going to zero at large separations
- Describing the bond breaking using a bond distance-dependent bond order and a bond order-dependent bond energy
- Including electrostatic and van der Waals interactions between all atoms (even bonded ones) because the valence bonds can break. Since the charges were distributed over the size of the atoms, coulombic interactions were shielded, going to a constant at short distances (point charges lead to infinities)

Thus, during MD simulations of reactive systems, many bonds may form or break.

All ReaxFF MD simulations were performed with 0.2 fs time steps to allow charges and bonds to be described properly as bonds were broken and formed.

We used 2.15 g/cm 3 carbon density in a three-dimensional periodic MD simulation box consisting of around 3,000 carbon atoms. This system was melted by heating to 6,000 K for 5 ps and then quenched to 300 K over 5.7 ps (1,000 K/ps), followed by equilibration at 300 K for 100 ps to obtain amorphous carbon. Then we introduced 3 graphitic layers on top of the amorphous carbon, heated to 3,500 K for 100 ps for equilibration, and quenched again to 300 K at 100 K/ps.

The surface layer was oxidized with 0%, 2.5%, 4.0%, and 12.0% oxygen to carbon ratios to simulate experimental observations. Here we used the ratios of functionalized C from experimental results. The hydrated ionomer was heated and equilibrated at 600 K for 100 ps and then cooled and further equilibrated at 300 K for 100 ps. Then the hydrated PFSA ionomer was placed on the top of the carbon surfaces having different oxidized graphitic surfaces and equilibrated for 200 ps at 300 K (12 $\rm H_2O/sulfonic~acid~[-SO_3^-]$) at the ionomer and carbon interface).

The interaction between the hydrated PFSA ionomer (based on the molecular structure of Nafion from previous simulations 49) and the carbon surface was calculated via energy minimization and equilibration. The interface energies were calculated by using Equation 4.

$$Interface\ energy(kcal/area) = \frac{(E_{Total}(carbon + Nafion) - E_{carbon}(carbon\ subs.) - E_{Nafion}(Nafion)\)}{Interface\ area}$$
 (Equation 4)

SUPPLEMENTAL INFORMATION

Supplemental Information can be found online at https://doi.org/10.1016/j.matt. 2020.09.025.

ACKNOWLEDGMENTS

Y.H., X.D., W.A.G., Z.Z., M.D.H., B.M., W.X., and Z. Liu. acknowledge support from the Office of Naval Research grant no. N00014-18-1-2155. Y.H., Z.Z., and Z. Liu. also





acknowledge the Defense University Research Instrumentation Program (DURIP) support by grant no. of N00014-18-1-2271. I.L. and F.Z. acknowledge financial support from the U.S. National Science Foundation (NSF), Division of Chemistry, under grant number CHE-1854439. W.A.G. thanks NSF (CBET-1805022) for partial support. The authors thank the Chemical Engineering & Fuel Cell Department of Ford Motor Company for assistance in MEA preparation and testing. This research used resources of the Advanced Light Source, which is a DOE Office of Science User Facility under contract no. DE-AC02-05CH11231. The authors thank the National Synchrotron Radiation Research Center (NSRRC) scientists for their skillful assistance during the synchrotron radiation XPS measurement. The authors thank Elena Kreimer (Director of Microanalytical Facility, College of Chemistry, University of California Berkeley) for helping with the CHNS elemental analysis. EDS mapping on JEOL Grand ARM was conducted using the facilities in the Irvine Materials Research Institute (IMRI) at the University of California Irvine.

AUTHOR CONTRIBUTIONS

Z.Z. and Y.H. conceived the idea and designed the experiments. Z.Z. conducted the materials preparation, characterization, and fuel cell test at UCLA. W.X., Z. Liu, and J.Z. contributed to the experiments at UCLA. M.D.H. and B.V.M. conducted the MD simulations, while Z. Luo and W.A.G. supervised the simulations. C.X., Z. Lu, and J.Y. conducted the fuel cell test in the Ford Motor Company. Y.-S.L. conducted the synchrotron-based NEXAFS experiment, and J.G. supervised the experiment. S.H.-H. performed the synchrotron-based XPS test. I.L. conducted the ATR-FTIR test, and F.Z. supervised the work. W.G. conducted the EDS mapping analysis, and X.P. supervised the work. Z.Z., X.D., and Y.H. wrote the paper with substantial input from other authors. Y.H. supervised the whole project.

DECLARATION OF INTERESTS

A US provisional patent, "High performance platinum-based catalyst combined with carbon support engineering" (application no. 62/905,564), has been filed by UCLA. The processing conditions and related characterization results of the carbon materials have been submitted for a patent application. The rest of the data and figures in this work have not been presented or published elsewhere.

Received: July 28, 2020 Revised: September 6, 2020 Accepted: September 28, 2020 Published: October 21, 2020

REFERENCES

- Weydahl, H., Gilljam, M., Lian, T., Johannessen, T.C., Holm, S.I., and Hasvold, J.Ø. (2019). Fuel cell systems for long-endurance autonomous underwater vehicles—challenges and benefits. Int. J. Hydrogen Energy 45, 5543–5553.
- Ustolin, F., and Taccani, R. (2018). Fuel cells for airborne usage: energy storage comparison. Int. J. Hydrogen Energy 43, 11853–11861.
- Debe, M.K. (2012). Electrocatalyst approaches and challenges for automotive fuel cells. Nature 486, 43–51.
- Kongkanand, A., Gu, W., and Mathias, M.F. (2017). Proton-exchange membrane fuel cells with low-Pt content. In Encyclopedia of

- Sustainability Science and Technology, R.A. Meyers, ed. (Springer New York), pp. 1–20.
- Kongkanand, A., and Mathias, M.F. (2016). The priority and challenge of high-power performance of low-platinum proton-exchange membrane fuel cells. J. Phys. Chem. Lett. 7, 1127–1137.
- Seh, Z.W., Kibsgaard, J., Dickens, C.F., Chorkendorff, I., Nørskov, J.K., and Jaramillo, T.F. (2017). Combining theory and experiment in electrocatalysis: insights into materials design. Science 355, eaad4998.
- Pedersen, C.M., Escudero-Escribano, M., Velázquez-Palenzuela, A., Christensen, L.H., Chorkendorff, I., and Stephens, I.E.L. (2015). Benchmarking Pt-based electrocatalysts for
- low temperature fuel cell reactions with the rotating disk electrode: oxygen reduction and hydrogen oxidation in the presence of CO (review article). Electrochim. Acta 179, 647–657.
- Xie, C., Niu, Z., Kim, D., Li, M., and Yang, P. (2020). Surface and interface control in nanoparticle catalysis. Chem. Rev. 120, 1184– 1249
- Jacob, T., and Goddard, W.A., III (2006). Water formation on Pt and Pt-based alloys: a theoretical description of a catalytic reaction. ChemPhysChem 7, 992–1005.
- 10. Zhang, Z., Luo, Z., Chen, B., Wei, C., Zhao, J., Chen, J., Zhang, X., Lai, Z., Fan, Z., Tan, C., et al. (2016). One-pot synthesis of highly anisotropic

Matter Article



- five-fold-twinned PtCu nanoframes used as a bifunctional electrocatalyst for oxygen reduction and methanol oxidation. Adv. Mater. 28 8712–8717
- Holdcroft, S. (2014). Fuel cell catalyst layers: a polymer science perspective. Chem. Mater. 26, 381–393.
- Weber, A.Z., and Kusoglu, A. (2014). Unexplained transport resistances for low-loaded fuel-cell catalyst layers. J. Mater. Chem. A 2, 17207–17211.
- Li, W., Chen, Z., Xu, L., and Yan, Y. (2010). A solution-phase synthesis method to highly active Pt-Co/C electrocatalysts for proton exchange membrane fuel cell. J. Power Sources 195, 2534–2540.
- Han, B., Carlton, C.E., Kongkanand, A., Kukreja, R.S., Theobald, B.R., Gan, L., O'Malley, R., Strasser, P., Wagner, F.T., and Shao-Horn, Y. (2015). Record activity and stability of dealloyed bimetallic catalysts for proton exchange membrane fuel cells. Energy Environ. Sci. 8, 258–266.
- Jia, Q., Caldwell, K., Strickland, K., Ziegelbauer, J.M., Liu, Z., Yu, Z., Ramaker, D.E., and Mukerjee, S. (2015). Improved oxygen reduction activity and durability of dealloyed PtCox catalysts for proton exchange membrane fuel cells: strain, ligand, and particle size effects. ACS Catal. 5, 176–186.
- 16. Li, J., Xi, Z., Pan, Y.-T., Spendelow, J.S., Duchesne, P.N., Su, D., Li, Q., Yu, C., Yin, Z., Shen, B., et al. (2018). Fe stabilization by intermetallic L10-FePt and Pt catalysis enhancement in L10-FePt/Pt nanoparticles for efficient oxygen reduction reaction in fuel cells. J. Am. Chem. Soc. 140, 2926–2932.
- Li, J., Sharma, S., Liu, X., Pan, Y.-T., Spendelow, J.S., Chi, M., Jia, Y., Zhang, P., Cullen, D.A., Xi, Z., et al. (2019). Hard-magnet L10-CoPt nanoparticles advance fuel cell catalysis. Joule 3. 124-135
- Yarlagadda, V., Carpenter, M.K., Moylan, T.E., Kukreja, R.S., Koestner, R., Gu, W., Thompson, L., and Kongkanand, A. (2018). Boosting fuel cell performance with accessible carbon mesopores. ACS Energy Lett. 3, 618–621.
- Inoue, G., and Kawase, M. (2016). Effect of porous structure of catalyst layer on effective oxygen diffusion coefficient in polymer electrolyte fuel cell. J. Power Sources 327, 1–10.
- Nonoyama, N., Okazaki, S., Weber, A.Z., Ikogi, Y., and Yoshida, T. (2011). Analysis of oxygentransport diffusion resistance in protonexchange-membrane fuel cells.
 J. Electrochem. Soc. 158, B416–B423.
- Kreuer, K.D., Schuster, M., Obliers, B., Diat, O., Traub, U., Fuchs, A., Klock, U., Paddison, S.J., and Maier, J. (2008). Short-side-chain proton conducting perfluorosulfonic acid ionomers: why they perform better in PEM fuel cells. J. Power Sources 178, 499–509.
- Yu, H., Roller, J.M., Mustain, W.E., and Maric, R. (2015). Influence of the ionomer/carbon ratio for low-Pt loading catalyst layer prepared by reactive spray deposition technology. J. Power Sources 283, 84–94.
- 23. Li, H., Tang, Y., Wang, Z., Shi, Z., Wu, S., Song, D., Zhang, J., Fatih, K., Zhang, J., Wang, H.,

- et al. (2008). A review of water flooding issues in the proton exchange membrane fuel cell. J. Power Sources 178, 103–117.
- Orfanidi, A., Madkikar, P., El-Sayed, H.A., Harzer, G.S., Kratky, T., and Gasteiger, H.A. (2017). The key to high performance low Pt loaded electrodes. J. Electrochem. Soc. 164, F418–F426.
- Ott, S., Orfanidi, A., Schmies, H., Anke, B., Nong, H.N., Hübner, J., Gernert, U., Gliech, M., Lerch, M., and Strasser, P. (2019). Ionomer distribution control in porous carbonsupported catalyst layers for high-power and low Pt-loaded proton exchange membrane fuel cells. Nat. Mater. 19, 77–85.
- Jang, S.S., Molinero, V., Çağın, T., and Goddard, W.A. (2004). Nanophasesegregation and transport in nafion 117 from molecular dynamics simulations: effect of monomeric sequence. J. Phys. Chem. B 108, 3149–3157.
- Sha, Y., Yu, T.H., Merinov, B.V., Shirvanian, P., and Goddard, W.A. (2011). Oxygen hydration mechanism for the oxygen reduction reaction at Pt and Pd fuel cell catalysts. J. Phys. Chem. Lett. 2, 572–576.
- Zhang, L., Ji, L., Glans, P.-A., Zhang, Y., Zhu, J., and Guo, J. (2012). Electronic structure and chemical bonding of a graphene oxide–sulfur nanocomposite for use in superior performance lithium–sulfur cells. Phys. Chem. Chem. Phys. 14, 13670–13675.
- Banerjee, S., Hemraj-Benny, T., Balasubramanian, M., Fischer, D.A., Misewich, J.A., and Wong, S.S. (2004). Ozonized singlewalled carbon nanotubes investigated using NEXAFS spectroscopy. Chem. Commun. (Camb.), 772–773, https://doi.org/10.1039/ B315390H. https://pubs.rsc.org/en/content/ articlelanding/2004/cc/b315390h/unauth#! divAbstract.
- Banerjee, S., Hemraj-Benny, T., Balasubramanian, M., Fischer, D.A., Misewich, J.A., and Wong, S.S. (2004). Surface chemistry and structure of purified, ozonized, multiwalled carbon nanotubes probed by NEXAFS and vibrational spectroscopies. ChemPhysChem 5, 1416–1422.
- Wang, W., Ruiz, I., Lee, I., Zaera, F., Ozkan, M., and Ozkan, C.S. (2015). Improved functionality of graphene and carbon nanotube hybrid foam architecture by UV-ozone treatment. Nanoscale 7, 7045–7050.
- O'Reilly, J.M., and Mosher, R.A. (1983). Functional groups in carbon black by FTIR spectroscopy. Carbon 21, 47–51.
- Prest, W.M., and Mosher, R.A. (1982). Fourier transform IR spectroscopic characterization of the functional groups on carbon black. In Colloids and Surfaces in Reprographic Technology, M. Hair and M.D. Croucher, eds. (American Chemical Society), pp. 225–247.
- Powell, C.J., and Jablonski, A. (2010). NIST Electron Inelastic-Mean-Free-Path Database— Version 1.2 (National Institute of Standards and Technology).
- Stariha, S., Macauley, N., Sneed, B.T., Langlois, D., More, K.L., Mukundan, R., and Borup, R.L. (2018). Recent advances in catalyst accelerated

- stress tests for polymer electrolyte membrane fuel cells. J. Electrochem. Soc. 165, F492–F501.
- Borup, R.L., Kusoglu, A., Neyerlin, K.C., Mukundan, R., Ahluwalia, R.K., Cullen, D.A., More, K.L., Weber, A.Z., and Myers, D.J. (2020). Recent developments in catalyst-related PEM fuel cell durability. Curr. Opin. Electrochem. 21, 192–200.
- Zhao, Z., Chen, C., Liu, Z., Huang, J., Wu, M., Liu, H., Li, Y., and Huang, Y. (2019). Pt-based nanocrystal for electrocatalytic oxygen reduction. Adv. Mater. 31, 1808115.
- Yoshida, T., and Kojima, K. (2015). Toyota MIRAI fuel cell vehicle and progress toward a future hydrogen society. Electrochem. Soc. Interface 24, 45–49.
- 39. Ozden, A., Shahgaldi, S., Li, X., and Hamdullahpur, F. (2019). A review of gas diffusion layers for proton exchange membrane fuel cells—with a focus on characteristics, characterization techniques, materials and designs. Prog. Energy Combust. Sci. 74, 50–102.
- Kusoglu, A., and Weber, A.Z. (2017). New insights into perfluorinated sulfonic-acid ionomers. Chem. Rev. 117, 987–1104.
- Kienitz, B., Kolde, J., Priester, S., Baczkowski, C., and Crum, M. (2011). Ultra-thin reinforced ionomer membranes to meet next generation fuel cell targets. ECS Trans. 41, 1521–1530.
- Cao, L., Zhao, Z., Liu, Z., Gao, W., Dai, S., Gha, J., Xue, W., Sun, H., Duan, X., Pan, X., et al. (2019). Differential surface elemental distribution leads to significantly enhanced stability of PtNi-based ORR catalysts. Matter 1, 1567–1580.
- Sulek, M., Adams, J., Kaberline, S., Ricketts, M., and Waldecker, J.R. (2011). In situ metal ion contamination and the effects on proton exchange membrane fuel cell performance. J. Power Sources 196, 8967–8972.
- 44. Melo, L.G.A., Hitchcock, A.P., Jankovic, J., Stumper, J., Susac, D., and Berejnov, V. (2017). Quantitative mapping of ionomer in catalyst layers by electron and X-ray spectromicroscopy. ECS Trans. 80, 275–282.
- Cullen, D.A., Koestner, R., Kukreja, R.S., Liu, Z.Y., Minko, S., Trotsenko, O., Tokarev, A., Guetaz, L., Meyer, H.M., Parish, C.M., et al. (2014). Imaging and microanalysis of thin ionomer layers by scanning transmission electron microscopy. J. Electrochem. Soc. 161, F1111–F1117.
- Wu, J., Zhu, X., West, M.M., Tyliszczak, T., Shiu, H.-W., Shapiro, D., Berejnov, V., Susac, D., Stumper, J., and Hitchcock, A.P. (2018). Highresolution imaging of polymer electrolyte membrane fuel cell cathode layers by soft X-ray spectro-ptychography. J. Phys. Chem. C 122, 11709–11719.
- Soboleva, T., Zhao, X., Malek, K., Xie, Z., Navessin, T., and Holdcroft, S. (2010). On the micro-, meso-, and macroporous structures of polymer electrolyte membrane fuel cell catalyst layers. ACS Appl. Mater. Interfaces 2, 375–384.
- Yu, P.T., Gu, W., Makharia, R., Wagner, F.T., and Gasteiger, H.A. (2006). The impact of carbon stability on PEM fuel cell startup and shutdown voltage degradation. ECS Trans. 3, 797-809.





- 49. Goddard, W., Merinov, B., van Duin, A., Jacob, T., Blanco, M., Molinero, V., Jang, S.S., and Jang, Y.H. (2006). Multi-paradigm multi-scale simulations for fuel cell catalysts and membranes. Mol. Simulat. 32, 251–268.
- Nowak, E., Combes, G., Stitt, E.H., and Pacek, A.W. (2013). A comparison of contact angle measurement techniques applied to highly porous catalyst supports. Powder Technol. 233, 52–64.
- Sarkar, A., Ghosh, A.K., and Mahapatra, S. (2012). Lauric acid triggered in situ surface modification and phase selectivity of calcium
- carbonate: its application as an oil sorbent. J. Mater. Chem. 22, 11113–11120.
- Ferraro, G., Fratini, E., Rausa, R., Fiaschi, P., and Baglioni, P. (2016). Multiscale characterization of some commercial carbon blacks and diesel engine soot. Energy & Fuels 30, 9859–9866.
- Baker, D.R., Caulk, D.A., Neyerlin, K.C., and Murphy, M.W. (2009). Measurement of oxygen transport resistance in PEM fuel cells by limiting current methods. J. Electrochem. Soc. 156, B991–B1003.
- 54. Garsany, Y., Atkinson, R.W., Gould, B.D., and Swider-Lyons, K.E. (2018). High power, Low-Pt membrane electrode assemblies for proton exchange membrane fuel cells. J. Power Sources 408, 38–45.
- 55. van Duin, A.C.T., Dasgupta, S., Lorant, F., and Goddard, W.A. (2001). ReaxFF: a reactive force field for hydrocarbons. J. Phys. Chem. A *105*, 9396–9409.
- Plimpton, S. (1995). Fast parallel algorithms for short-range molecular dynamics. J. Comput. Phys. 117, 1–19.